Defect Engineering of *n*-Type Bi_2SeO_2 Thermoelectrics

Andrei Novitskii,[a,†] Michael Y. Toriyama,[b,†] Illia Serhiienko,[a,c] Takao Mori,[a,c,*] G. Jeffrey Snyder,[b] Prashun Gorai[d,e,*]

Bi_2SeO_2 is a promising *n*-type semiconductor to pair with *p*-type BiCuSeO in a thermoelectric (TE) device. The TE figure of merit zT and, therefore, the device efficiency must be optimized by tuning the carrier concentration. However, electron concentrations in self-doped *n*-type Bi_2SeO_2 span several orders of magnitude, even in samples with same nominal compositions. Such unsystematic variations in the electron concentration has a thermodynamic origin related to the variations in native defect concentrations. In this study, we use first-principles calculations to show that the selenium vacancy, which is the source of *n*-type conductivity in Bi_2SeO_2, varies by 1–2 orders of magnitude depending on the thermodynamic conditions. We predict that the electron concentration can be enhanced by synthesizing under more Se-poor conditions and/or at higher temperatures (T_{SSR}), which promote the formation of selenium vacancies without introducing extrinsic dopants. We validate our computational predictions through solid-state synthesis of Bi_2SeO_2. We observe more than two orders of magnitude increase in the electron concentration by solely adjusting the synthesis conditions. Additionally, we reveal the significant effect of grain boundary scattering on electron transport in Bi_2SeO_2, which is controlled by adjusting T_{SSR}. By simultaneously optimizing the electron concentration and mobility, we achieve a zT of ∼0.2 at 773 K for self-doped *n*-type Bi_2SeO_2. Our study highlights the need for careful control of thermodynamic growth conditions and demonstrates TE performance improvement by varying synthesis parameters.

1 Introduction

Thermoelectric (TE) materials utilize the Seebeck effect for solid-state conversion of heat to electricity.[1] The figure of merit (zT) is a measure of the TE performance of a material and is given by $zT = \alpha^2\sigma T/\kappa_{tot}$, where α, σ, κ_{tot} and T are the Seebeck coefficient, electrical conductivity, total thermal conductivity, and temperature, respectively. κ_{tot} is the sum of the electronic and lattice (phonon) contributions ($\kappa_{tot} = \kappa_{el} + \kappa_{lat}$). Layered oxychalcogenides are promising TE materials[2–4] due to their high-temperature chemical and structural stability, relatively high Seebeck coefficient, and intrinsically low κ_{lat}.[5] *p*-type BiCuSeO, is a well-known mid-temperature TE material,[6] with zT reaching a maximum of 1.5 at 873 K.[7,8] We need both *p*-type and *n*-type legs to build a TE device. It would be ideal to use the same material as the *p- and n*-type legs to avoid device failure due to different coefficients of thermal expansion and other issues. While *p*-type BiCuSeO exhibits relatively high TE performance, it is challenging to obtain *n*-type BiCuSeO.[9] Attempts to dope BiCuSeO *n*-type with halogens,[10–12] and transition metals,[8,13] have resulted in either low power factors and/or anomalous *p*-*n*-*p* transitions in the conductivity type with T. Therefore, an alternative *n*-type material is needed to pair with *p*-type BiCuSeO in a TE device.

Bi_2SeO_2 has emerged as a potential *n*-type material to pair with *p*-type BiCuSeO in TE devices. The crystal structure of Bi_2SeO_2 can be thought of as BiCuSeO-derived with missing Cu. Bi_2SeO_2 is known to be natively self-doped *n*-type.[14] Pan, et al., demonstrated a TE module of *p*-type BiCuSeO and *n*-type Bi_2SeO_2 with a maximum device ZT of 0.8 at 793 K.[15] The material zT of *n*-type Bi_2SeO_2 is lower than *p*-type BiCuSeO. To improve device efficiency, zT of each leg must be optimized, particularly through charge carrier optimization. Although the electron concentration in Bi_2SeO_2 in the aforementioned device was optimized through a mechanical shear exfoliation method,[15] other routes have also been adopted. Substituting Bi with Sb[16] and La,[17] Ge,[18,19] Sn,[20] Ti,[21] Ce,[22] Nb[23,24] and Ta,[25] has been successful to various degrees, either due to an increase in the electron concentration, change in the effective mass, or a combination of both. Substituting Se or O with S,[26] Te,[27,28] and Cl[29] has increased zT compared to self-doped Bi_2SeO_2. The highest zT of 0.69 at 773 K was achieved by Te substitution obtained through a mechanical shear exfoliation technique,[15,28] which was claimed to increase the concentration of donor-like Se vacancies (V_{Se}) leading to a sixfold enhancement in the power factor.

TE materials are often optimized through defect engineering, which can increase (or decrease) the concentration of charge carriers and decrease κ_{lat} through increased phonon scattering. The formation of point defects is strongly influenced by the synthesis conditions, including the reaction temperature. As a result, the reported electron concentrations in self-doped *n*-type Bi_2SeO_2 span several orders of magnitude (10^{15} – 10^{19} cm^{-3}) even in materials with the same nominal composition. Bi_2SeO_2 synthesis typically involves a solid-state reaction step, where one procedure uses a two-step method with different reaction temperatures and holding times,[18,25,30] while another uses a single solid-state reaction step at a fixed temperature.[26] A fundamental question arises: are these different synthesis procedures responsible for the wide variations in the reported electron concentrations and therefore, the TE performance of Bi_2SeO_2? For practical purposes, how do we systematically tune the electron concentration and improve the TE performance?

First-principles defect modeling can reveal the thermodynamic origin of the variations in defect-dependent material properties, including doping preference,[31] ionic conductivity,[32] dielectric properties,[33] etc. In this work, we combine density functional theory (DFT) calculations and solid-state synthesis to show that the wide variations in the reported electron concentrations of *n*-type Bi_2SeO_2 are due to unsystematic changes in the point defect

---

[a] ~~WPI-~~MANA, National Institute for Materials Science (NIMS), Tsukuba, Ibaraki 305-0044, Japan. [b] Northwestern University, Evanston, IL 60208, USA. [c] Graduate School of Pure and Applied Sciences, University of Tsukuba, Tsukuba, Ibaraki 305-8573, Japan. [d] Colorado School of Mines, Golden, CO 80401, USA. [e] Rensselaer Polytechnic Institute, NY 12180, USA. [†] These authors contributed equally. [*] E-mail: MORI.Takao@nims.go.jp, goraip@rpi.edu.

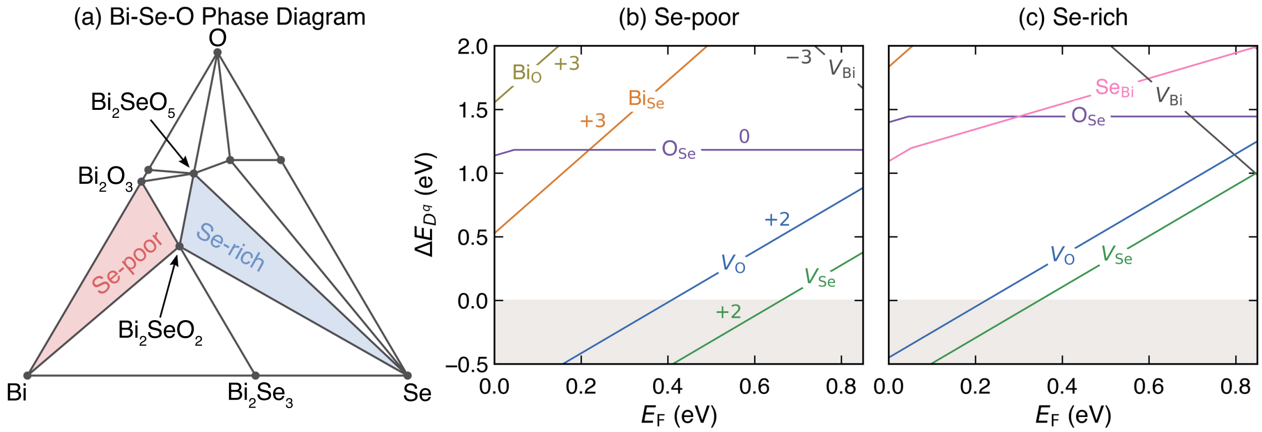

Figure 1 (a) Calculated phase diagram of the Bi-Se-O ternary composition space. Bi_2SeO_2 phase equilibria corresponding to the most Se-rich and most Se-poor thermodynamic conditions are highlighted. The calculated formation energy ($\Delta E_{D,q}$) of vacancy and antisite defects in Bi_2SeO_2 are shown for (b) most Se-poor condition, where Bi_2SeO_2 is in equilibrium with Bi and Bi_2O_3, and (c) most Se-rich condition, where Bi_2SeO_2 is in equilibrium with Se and Bi_2SeO_5. $\Delta E_{D,q}$ of V_{Se} is lowest and highest under the most Se-poor and Se-rich conditions, respectively.

concentrations and grain boundary scattering of charge carriers. We show that the solid-state reaction temperature (T_{SSR}) and elemental chemical potential (Se concentration) are accessible experimental knobs for controlling defect formation, grain boundary scattering, and TE performance of Bi_2SeO_2. Ultimately, by adjusting only the synthesis parameters, we achieved zT of 0.2 at 773 K for n-type self-doped Bi_2SeO_2.

2 Results and Discussion

2.1 Defect Chemistry of Bi_2SeO_2

Charged defects are the source of electronic carriers (electrons, holes) in semiconductors, and their concentrations directly affect the electronic carrier concentrations. The defect concentration depends on two parameters – formation energy ($\Delta E_{D,q}$) and temperature. Here, the temperature is typically the synthesis temperature at which the defects are sufficiently mobile to allow equilibration. Among other factors, $\Delta E_{D,q}$ also depends on the thermodynamic phase equilibrium.[31,32] In principle, both the temperature and phase equilibrium can be tuned by adjusting the synthesis conditions, enabling control over defect formation, and consequently, the electronic carrier concentration. To guide the optimization of the TE properties of Bi_2SeO_2, we computed the formation energetics of native defects using first-principles defect calculations. The computational methodology is discussed in Section 4. The goal is to identify experimental synthesis conditions that maximize electron concentration in n-type Bi_2SeO_2.

Figure 1(a) shows the calculated equilibrium phase diagram in the ternary Bi-Se-O chemical space. There are 5 distinct phase equilibria regions of Bi_2SeO_2, corresponding to the triangles around Bi_2SeO_2. $\Delta\mu_i$ are determined by the phase stability of Bi_2SeO_2 in the grand potential phase diagram and it captures the synthesis conditions, e.g., Se-rich and Se-poor growth conditions. The elemental chemical potentials ($\Delta\mu_i$) in each of these three-phase equilibria are listed in Table S1.

$\Delta E_{D,q}$ depends on $\Delta\mu_i$ (Eq. 5). Figure 1 shows $\Delta E_{D,q}$ plotted as a function of the Fermi energy (E_F) under two limiting synthesis conditions – Se-poor (equilibrium with elemental Bi and Bi_2O_3) and Se-rich (equilibrium with elemental Se and Bi_2SeO_5). We find that under both conditions, selenium vacancies (V_{Se}) are the dominant defects with lowest $\Delta E_{D,q}$, followed by oxygen vacancies (V_O). Both V_{Se} and V_O are shallow donors, i.e., they donate free electrons and are responsible for the n-type conduction in self-doped Bi_2SeO_2. $\Delta E_{D,q}$ of V_{Se} is the lowest under Se-poor synthesis conditions (Figure 1b) and the highest under Se-rich conditions (Figure 1c), but regardless of the synthesis conditions, Bi_2SeO_2 remains an n-type material. The low $\Delta E_{D,q}$ of the donor V_{Se} and V_O imply that Bi_2SeO_2 cannot be doped p-type because the holes generated by the acceptor dopant will be charge-compensated by the electrons produced by the native donor defects.

The free electron concentration (n) in Bi_2SeO_2 is principally determined by the formation energy of donor-like V_{Se}, which is different for each phase equilibrium condition. Therefore, we predict a *range* of n at a given synthesis temperature (Figure 2). The upper bound of n is determined by the most Se-poor condition (lowest V_{Se} formation energy) and the lower bound by the most Se-rich condition (highest V_{Se} formation energy). The measured n for single-crystal Bi_2SeO_2 are within the range calculated with DFT. However, the measured n in polycrystalline samples vary between 10^{15} and 10^{19} cm^{-3}, and in many cases, fall outside the DFT calculated range. We attribute this discrepancy to the presence of grain boundaries in polycrystalline samples, which can act as sources or sinks of electronic carriers. For example, atom probe tomography showed evidence that Mg-deficient grain boundaries in Mg_3Sb_2 can deplete free electrons from the material, thus lowering its concentration relative to the grains.[34] Our predictive defect model does not account for extended defects such as grain boundaries, which could explain the discrepancy between the measured and calculated n.

The large variations in n for polycrystalline samples are presumably due to the differences in the microstructure arising from different processing conditions , e.g., ball milling, shear exfoliation, different atmospheres during the solid-state reaction,

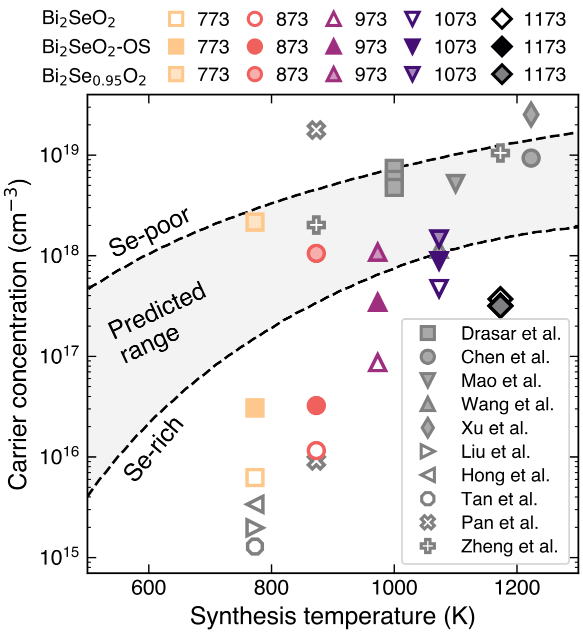

Figure 2 The charge carrier concentration of Bi_2SeO_2 as a function of synthesis temperature. The upper and lower bounds (black dashed lines) of the free electron concentration are predicted from DFT defect calculations under Se-poor and Se-rich conditions, respectively. Experimentally measured n values obtained in this work are shown as open (Bi_2SeO_2), solid (Bi_2SeO_2 fabricated by one-step solid-state reaction), and filled ($Bi_2Se_{0.95}O_2$) symbols, respectively. Literature data for single crystals (filled gray symbols) and polycrystals (open gray symbols) is also shown for comparison (Drasar et al.,[35] Chen et al.,[36] Mao et al.,[37] Wang et al.,[38] Xu et al.,[39] Liu et al.,[18] Hong et al.,[22] Tan et al.,[25] Pan et al.,[15] Zheng et al.[30]).

etc.[15,25,30] For example, Pan et al. increased n from $\sim 10^{16}$ cm^{-3} to $\sim 10^{19}$ cm^{-3} using a shear exfoliation technique,[15] which is claimed to form a high concentration of V_{Se}, even higher than the equilibrium concentrations predicted by our defect calculations. Similarly, synthesis conditions that allow more Se evaporation (vs. conditions with limited Se ventilation) will create Se-poor environments that promote the formation of V_{Se} and increase n. For example, Zheng et al. conducted solid-state synthesis on powders of Bi_2SeO_2 rather than cold-pressed pellets, which caused Se evaporation due to relatively poor mixing.[30]

In order to engineer the TE properties of Bi_2SeO_2 rationally, defects must be controlled systematically. The V_{Se} concentration and, therefore, n can be controlled by (1) tuning the synthesis temperature, and (2) changing the synthesis condition (Se-rich vs. Se-poor). Since many recipes for Bi_2SeO_2 involve a solid-state reaction step, an accessible experimental knob for tuning n is the solid-state reaction temperature (T_{SSR}). Moreover, the nominal composition can be varied to explore TE properties under Se-rich and Se-poor conditions. In the following sections, we show the effects of modifying thermodynamic conditions on the microstructure, n, and TE properties.

2.2 Structural and Microstructural Properties

We synthesize two series of samples, one with a nominally stoichiometric composition of Bi_2SeO_2, and another with a nominal composition of $Bi_2Se_{0.95}O_2$. Both series were synthesized through a two-step solid-state reaction followed by spark plasma sintering (SPS), as detailed in Section 4. To reveal the effect of processing conditions during the solid-state reaction, samples with a nominal composition of Bi_2SeO_2 were also obtained using a one-step procedure (see Section 4 for details). Since the data obtained for this series of samples are similar to those for Bi_2SeO_2 obtained by a two-step solid-state reaction, it is mainly presented in the Supporting Information. To explore the effects of synthesis temperature, we vary the solid-state reaction temperature (T_{SSR}) from 773 K to 1173 K for each series.

The room-temperature X-ray powder diffraction (XRD) patterns of all samples are displayed in Figure 3 and Figure S1. All the main diffraction peaks correspond to the Bi_2SeO_2 phase with the tetragonal $(Na_{0.25}Bi_{0.75})_2O_2Cl$-type structure and $I4/mmm$ space group.[40] In nominally stoichiometric samples, no secondary phases are discernible (Figures 3a, S1). Thus, within the detection limit of XRD, we can confirm that all specimens, regardless of T_{SSR} and number of steps during reaction, exhibit a pristine Bi_2SeO_2 phase. The actual composition and the distribution of elements examined by energy-dispersive X-ray spectroscopy (EDS) indicate that all the elements are homogeneously distributed, and the actual compositions are similar to the nominal ones for all the samples among both the one-step and two-step series of Bi_2SeO_2 (Figures S2 – S6).

In the relatively Se-poor samples synthesized with a nominal composition of $Bi_2Se_{0.95}O_2$, however, peaks corresponding to Bi_2O_3 impurities are evident near 27° in the XRD patterns (Figure 3c). In fact, trace amounts of both Bi_2O_3 and elemental Bi can be found in EDS measurements (Figures S2 – S6), indicating that these samples exist in the three-phase equilibrium region labeled “Se-poor” in Figure 1a. However, while remaining in the three-phase region, it seems that the ratio of secondary phases in these samples changes with increasing T_{SSR}, as indicated by the variations in intensities in the XRD patterns (Figure 3c). While the intensities of monoclinic Bi_2O_3 decrease with increasing T_{SSR}, for the sample with $T_{SSR} = 1173$ K, reflections from cubic and/or tetragonal Bi_2O_3 also become visible near 28°, as can be expected when Bi_2O_3 is heated above 1030 K.[41]

As T_{SSR} increases, there is a noticeable increase in the relative intensities of $(00l)$ peaks shown in the XRD patterns (Figures 3a, b, S7). This suggests a preferential orientation of the crystallites, which is commonly observed in layered oxyselenides following a uniaxial densification process.[42,43] Indeed, in contrast to the samples obtained at $T_{SSR} = 773$ K with randomly arranged platelet grains (Figure 3d), the grains of the samples synthesized at $T_{SSR} = 1173$ K are more aligned along a single direction (Figure 3e). The degree of ab orientation for the $(00l)$ crystal planes, termed as $F_{(00l)}$ and determined using the Lotgering method, rises from slightly less than 0.05 at $T_{SSR} = 773$ K to just over 0.25 at $T_{SSR} = 1173$ K (Figure S7), further supporting preferential grain orientation in the samples. Interestingly, along

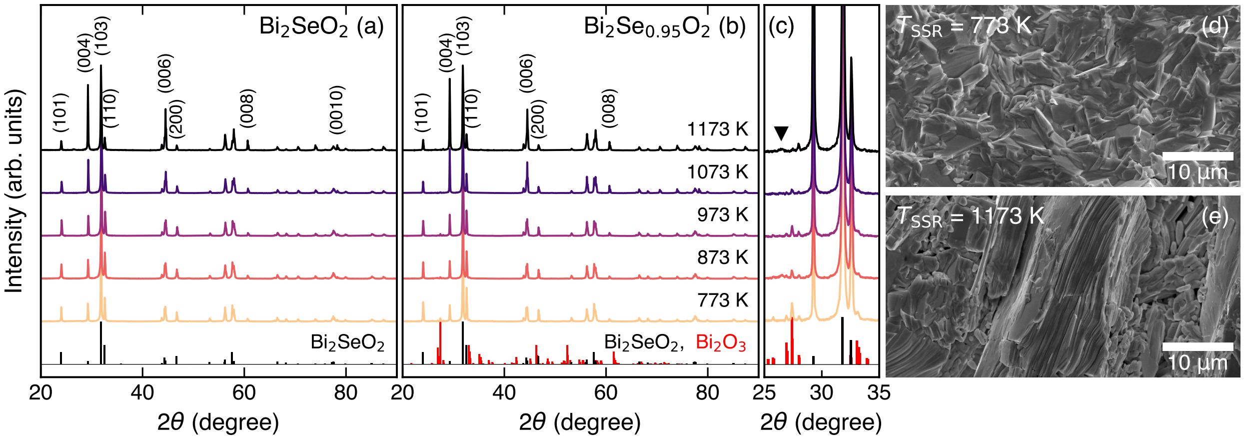

Figure 3 Room temperature X-ray diffraction patterns of (a) Bi_2SeO_2 and (b) $Bi_2Se_{0.95}O_2$ samples prepared by two-step solid-state reaction. (c) Magnified section of (b) in a 2θ range from 25° to 35° to show the most intensive reflections corresponding to Bi_2O_3. In (c), the main diffraction peak of the Bi phase is also indicated by a black triangle (▼). SEM micrographs of the fracture surface for Bi_2SeO_2 obtained at (d) T_{SSR} = 773 K and (e) T_{SSR} = 1173 K, respectively.

with a more pronounced preferred orientation, the grain size also proportionally increases with rising T_{SSR}, but only in the in-plane direction; meanwhile, the thickness of platelet-like grains slightly decreases from 400 – 600 nm (T_{SSR} = 773 K) to 200 – 400 nm (T_{SSR} = 1173 K), as shown in Figures 3d and 3e. Note that the stronger intensities of the $(00l)$ peaks with increasing T_{SSR} (Figures 3a, b) may also suggest an increase in the concentration of V_{Se}, as the $I_{(004)}/I_{(101)}$ ratio is dependent on the Se content.[44]

2.3 Experimental Carrier Concentration

In the nominally stoichiometric series synthesized using the two-step solid-state reaction procedure, we observe a gradual increase in carrier concentration (n) with increasing T_{SSR}, from $\sim 6 \times 10^{15}$ cm^{-3} at T_{SSR} = 773 K to $\sim 4 \times 10^{17}$ cm^{-3} at T_{SSR} = 1173 K (Figure 2). This is consistent with the DFT prediction that increasing the synthesis temperature will increase n, suggesting that more V_{Se} defects are being generated with increasing T_{SSR}. A similar increase in n with T_{SSR} is observed in Bi_2SeO_2 synthesized using the one-step solid-state reaction process (Figure 2).

Interestingly, n of the one-step sub-series are slightly higher than those of the two-step sub-series, and this difference diminishes as T_{SSR} increases (Figure 2). The difference in n can be attributed to the thermodynamic conditions established by the two reaction series. Se does not have sufficient time to react with Bi during the one-step solid-state reaction,[30] whereas most Se reacts with Bi and forms an intermediate Bi_2Se_3 phase during the initial heating stage at 573 K in the two-step process. Bi_2SeO_2 is therefore in a slightly more Se-rich state when synthesized with a two-step solid-state reaction than with a one-step process, which lowers n. At higher T_{SSR}, the difference in n between the one-step and two-step sub-series reduces because Se can evaporate from Bi_2SeO_2 more readily. At the same time, n for the samples obtained at T_{SSR} = 1173 K is slightly lower compared to that at T_{SSR} = 1073 K. This could be attributed to the Se-rich environment formed in the sealed tubes during the solid-state reaction at high T_{SSR}.

The $Bi_2Se_{0.95}O_2$ samples exhibit higher n than the stoichiometric samples (Figure 2). This observation is consistent with the higher concentration of V_{Se} defects, arising from the lower formation energy of V_{Se} under Se-poor conditions (Figure 1b) compared to Se-rich conditions (Figure 1c). Despite the larger concentration of V_{Se} in the $Bi_2Se_{0.95}O_2$ samples, we find that n decreases slightly with T_{SSR}, contrary to the stoichiometric series where n increases with T_{SSR}. It is unclear what is causing the inverse trend between n and T_{SSR} in the $Bi_2Se_{0.95}O_2$ samples, as it can arise from numerous factors such as defect equilibration during the SPS step of the synthesis instead of the solid-state reaction step, the temperature dependence of the elemental chemical potentials $\Delta\mu_i$, or free carriers from the impurity phases Bi_2O_3 and elemental Bi. Nonetheless, our results confirm that synthesizing Bi_2SeO_2 under slightly Se-poor conditions (in this case, nominally $Bi_2Se_{0.95}O_2$) can raise n compared to a stoichiometric composition, especially at lower solid-state reaction temperatures (Figure 2).

2.4 Electrical Transport Properties

We analyze the evolution of electrical transport properties in our samples using a single parabolic band transport model, which is appropriate for Bi_2SeO_2 given the nearly parabolic conduction band obtained from DFT (Figure S8). We studied the Seebeck coefficient (α) as a function of electrical conductivity (σ) and carrier concentration (n) as shown in Figure 4. For semiconductors with a chemical potential $\eta \leq 1$ ($|\alpha| \geq 150$ µV K^{-1}), the relationship between α and n (or σ) can be described by the Pisarenko formula:[1]

$$\alpha = \pm \frac{k_B}{e} \left[r + \frac{5}{2} + \ln \left(\frac{2(2\pi m_d^* k_B T)^{3/2}}{h^3 n} \right) \right] \tag{1}$$

or

$$\alpha = \pm \frac{k_B}{e} \left[r + \frac{5}{2} + \ln \left(\Gamma \left(r + \frac{5}{2} \right) \sigma_{E_0} \right) - \ln \sigma \right], \tag{2}$$

where k_B is the Boltzmann constant, e is the electron charge, r is the scattering factor ($r = -1/2$ for acoustic phonon scattering), m_d^* is the density-of-states effective mass, h is the Planck's constant, Γ is the gamma function, and σ_{E_0} is the transport coefficient, which is merely a function of the weighted mobility:[45]

$$\sigma_{E_0} = \frac{8\pi e\left(2\pi m_e k_B T\right)^{3/2}}{3h^3}\mu_w. \tag{3}$$

Here, μ_w is the weighted mobility given by $\mu_w = \mu_0\left(m_d^*/m_e\right)^{3/2}$, where μ_0 represents the intrinsic carrier mobility, and m_e is the electron mass.

Figure 4 shows the Pisarenko (Figure 4a) and Jonker (Figure 4b) plots for Bi_2SeO_2 samples from the literature as well as those studied in the present work. In agreement with single parabolic band transport and previous reports,[14] the effective mass is estimated to be $m_d^* \approx 0.2$ for all the samples (Figure 4a). At the same time, the electrical transport properties of Bi_2SeO_2 and $Bi_2Se_{0.95}O_2$ are clearly modified by tuning T_{SSR} (Figures 4, 5). The negative α confirms the n-type conduction, i.e., electrons are the majority charge carriers. At room temperature, there is a twofold decrease in α of the Bi_2SeO_2 samples as T_{SSR} and, consequently, n increases (Figures 4, S9a). Simultaneously, the room-temperature σ increases by nearly three orders of magnitude by elevating T_{SSR} from 773 K to 1173 K (Figures 4b, S9b), consistent with the increase in n (Figure 2). The optimized balance between σ and α leads to a nearly two order of magnitude improvement in the power factor ($\alpha^2\sigma$) as the solid-state reaction temperature increases from 773 K to 1173 K (Figure S9c).

The weighted mobility of Bi_2SeO_2 samples also increases with T_{SSR} (Figure 4b), which are at odds with the single parabolic band model. Typically, charge carrier mobility decreases when carrier density increases in semiconductors. The weighted mobility (μ_w) and Hall mobility (μ_H), however, both unexpectedly increase by over an order of magnitude with elevated T_{SSR} (Figure S10). Indeed, μ_w of Bi_2SeO_2 varies from less than 10^{-1} cm^2 V^{-1} s^{-1} for fine-grained polycrystalline samples to almost 10^2 cm^2 V^{-1} s^{-1} for single crystals despite comparable carrier density level (Figure 4b). The temperature dependence of μ_w can be used to reveal the main charge carrier scattering mechanism, in a similar way to the analysis of $\mu_H(T)$.[45] A closer look at $\mu_w(T)$ indeed indicates changes in electron scattering (Figure S11). Similar to Mg_3Sb_2 and $SrTiO_3$,[46,47] it seems that grain boundary scattering plays an important role in the charge carrier transport of Bi_2SeO_2. Grain boundary resistance is also evident from the increase in σ with measurement temperature (not to be confused with T_{SSR}) at $T < 500$ K for samples obtained at T_{SSR} below 973 K (Figure 5a). Se-poor $Bi_2Se_{0.95}O_2$ samples, in turn, show far less thermally-activated conductivity near room temperature (Figure 5a). Moreover, samples synthesized at higher T_{SSR} exhibit reduced grain boundary scattering (Figure S11). This reduction allows μ_w and μ_H to approach values similar to those of single crystals (Figures 4b, S10). All of the aforementioned make charge carrier mobility the main reason behind the increase in σ of $Bi_2Se_{0.95}O_2$ from 14 Ω^{-1} cm^{-1} (T_{SSR} = 773 K) to 36 Ω^{-1} cm^{-1} (T_{SSR} = 1073 K) at room temperature (Figure S9b), while α is only slightly affected by changes in T_{SSR} (Figures 5b, S9a). Interestingly, similar changes in the temperature dependence of electrical conductivity were also observed in the study of Pan et al.,[15] where the activated behavior of $\sigma(T)$ was suppressed with an increase in shear-exfoliation time. The authors did not discuss this in detail, but the reduction in grain boundary scattering might be another reason for shear-exfoliated Bi_2SeO_2 to exhibit higher zT values, in addition to the significant increase in V_{Se} concentration.[15,28]

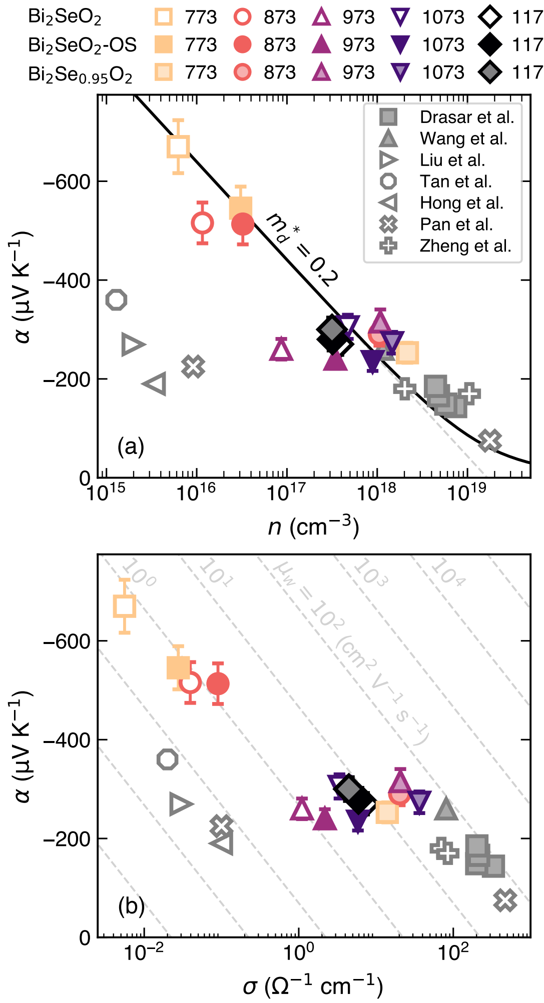

Figure 4 Room temperature Seebeck coefficient versus (a) carrier concentration (Pisarenko plot) and (b) electrical conductivity (Jonker plot) for Bi_2SeO_2 (open symbols) and $Bi_2Se_{0.95}O_2$ (filled solid symbols) samples fabricated by a two-step solid-state reaction at different temperatures. Data for Bi_2SeO_2 fabricated by a one-step solid-state reaction is also presented (solid symbols). The solid line in (a) represents the Seebeck coefficient calculated in the framework of the single parabolic band model, assuming acoustic phonon scattering ($r = -1/2$) and $m_d^* = 0.2$. The dashed lines in (b) represent the Pisarenko formula (Eq. 2) for different weighted mobility values (μ_w in cm^2 V^{-1} s^{-1}), each labeled next to its corresponding curve at the top part of the figure. For comparison, literature data for both single crystals (filled gray symbols) and polycrystals (open gray symbols) are also shown (Drasar et al.,[35] Wang et al.,[38] Liu et al.,[18] Hong et al.,[22] Tan et al.,[25] Pan et al.,[15] Zheng et al.[30]).

Overall, there are noticeable difference in the transport properties between Se-poor $Bi_2Se_{0.95}O_2$ samples and nominally stoichiometric Bi_2SeO_2 samples. Our results demonstrate that carefully controlling thermodynamic conditions (chemical potential, temperature) during the synthesis of Bi_2SeO_2 allows independent control of both charge carrier concentration (n) and mobility (μ). Simultaneous optimization of n and reduction of grain boundary scattering by shifting synthesis conditions to Se-poor and increasing T_{SSR} have resulted in a sizeable improvement of the power factor across the entire temperature range studied (Figure S12).

2.5 Thermal Transport and Thermoelectric Efficiency

The total thermal conductivity (κ_{tot}) monotonically decreases with temperature for all the samples, reaching nearly 1 W m^{-1} K^{-1} or below at 773 K (Figure 5c). For the Bi_2SeO_2 sample obtained at T_{SSR} = 1173 K, κ_{tot} reaches its lowest values, approaching the glassy limit (≈ 0.55 W m^{-1} K^{-1})[48] at 773 K. To further understand the thermal transport in Bi_2SeO_2, we examine both the lattice (κ_{lat}) and electronic (κ_{el}) contributions to κ_{tot} using the Wiedemann-Franz law, as described in Section 4. The electronic contribution does not exceed 3% even for $Bi_2Se_{0.95}O_2$ samples (which have high σ), indicating that the κ_{tot} is predominantly determined by the lattice contribution. Furthermore, our analysis reveals that point defects are the dominant phonon scattering mechanism as $\kappa_{lat}(T)$ follows a $T^{-0.6}$ dependence for all samples (Figure S12).

In Bi_2SeO_2 samples in particular, a considerable drop in κ_{tot} by more than 30% upon increasing T_{SSR} is observed (Figure S9d), which can be attributed to the increase in V_{Se} concentration. This substantial reduction in κ_{tot} is comparable to, and even surpasses, the reported reduction in κ_{tot} for conventionally-doped Bi_2SeO_2.[17,18,22,25,27] This becomes possible due to the high efficacy of vacancy defects as scattering centers in contrast to substitutional atoms. The formation of vacancies involves the complete removal of bonds to the neighboring atoms, which introduces strong mass and strain fluctuations and decreases κ_{lat}.[49,50] On the other hand, κ_{tot} of Se-poor $Bi_2Se_{0.95}O_2$ samples slightly increases with increase in T_{SSR} (Figure S9d). This is consistent with the discussion presented in Sections 2.3 and 2.4, suggesting that the V_{Se} concentration does not vary significantly in $Bi_2Se_{0.95}O_2$ samples upon increasing T_{SSR}. In the Se-poor samples, the main effect of increasing T_{SSR} is the corresponding grain growth, which is most likely the origin of the observed increase in κ_{tot}.

We achieve a peak zT of 0.15 – 0.2 at 773 K for Bi_2SeO_2 samples obtained at T_{SSR} = 1073 K and 1173 K, as well as Se-poor $Bi_2Se_{0.95}O_2$ samples obtained at T_{SSR} below 1173 K (Figure 5d). These are some of the highest zT values reported thus far for undoped Bi_2SeO_2 obtained with solid-state reaction synthesis, which typically reaches $zT \leq 0.1$.[15,17,18,22,25,27] The improvement in zT can be understood through the quality factor $\beta \propto \mu_w/\kappa_{lat}$, which determines the maximum zT achievable for a given carrier concentration at a specific temperature.[1,51] In Bi_2SeO_2, increasing T_{SSR} generates more V_{Se}, resulting in a higher weighted mobility (Figure S9e) and lower lattice thermal conductivity (Figure S9d). As a result, the quality factor β is enhanced with T_{SSR} (Figure S9f), and a higher zT is achieved (Figure S14). Such a noticeable improvement of μ_w is possible due to the simultaneous optimization of charge carrier concentration and the reduction of grain boundary scattering, as discussed in detail in Section 2.4. In turn, even more pronounced suppression of grain boundary scattering in Se-poor samples correspondingly leads to a more substantial increase in μ_w (Figure 4b). Consequently, β is also significantly improved despite a slight increase in κ_{lat} of $Bi_2Se_{0.95}O_2$ with T_{SSR} (Figure S9d). Although this does not lead to a significantly higher zT_{max} value, it still improves zT at low temperatures

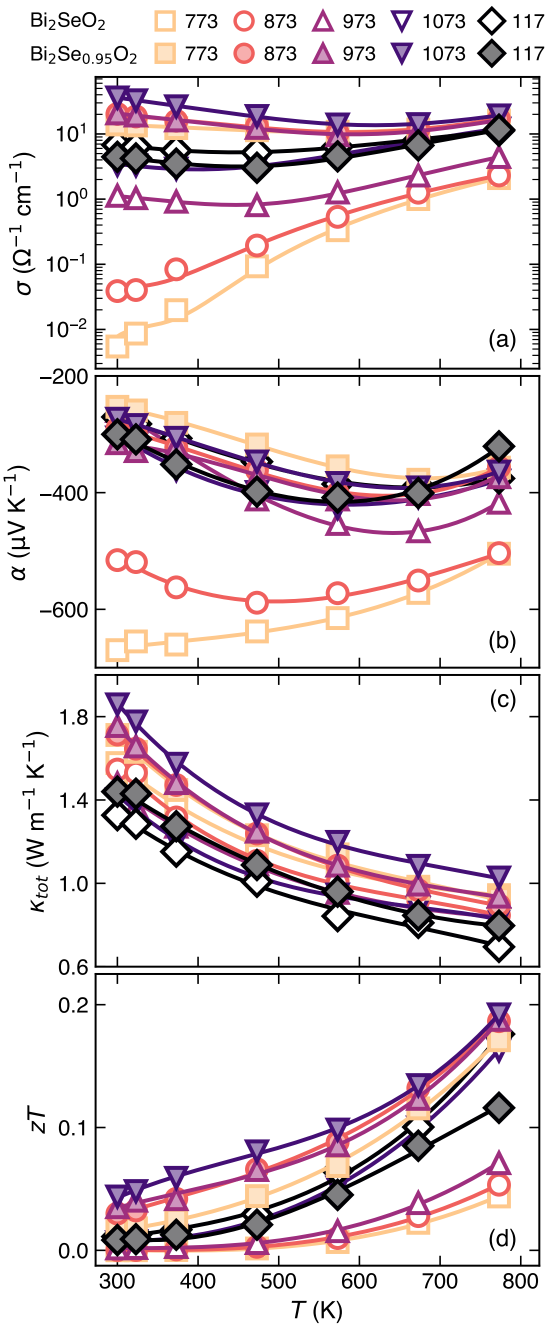

Figure 5 Temperature dependence of the (a) electrical conductivity σ, (b) Seebeck coefficient α, (c) total thermal conductivity κ_{tot}, and (d) the figure of merit zT for Bi_2SeO_2 samples fabricated by one-step (solid symbols) and two-step (open symbols) solid-state reactions.

(Figure 5d), thereby leading to higher ZT_{av} in $Bi_2Se_{0.95}O_2$.

3 Conclusions

The development of efficient n-type oxyselenide-based TE materials requires precise control of native defects. In this work, we combine theory and experiment to demonstrate that TE properties and performance in n-type Bi_2SeO_2 can be improved by systematically controlling defect formation with synthesis conditions. We predict that V_{Se} is the main source of n-type conductivity, and that the free electron concentration can be increased with the synthesis temperature and/or shifting thermodynamic conditions from Se-rich to Se-poor. Experiments largely confirm these predictions. When the solid-state reaction temperature (T_{SSR}) is elevated, nominally stoichiometric samples of Bi_2SeO_2 exhibit enhanced electron concentration n and reduced grain boundary scattering, thus improving the power factor. A suppression in thermal conductivity is also observed, consistent with the higher V_{Se} content at higher T_{SSR}. Relatively Se-poor samples (with nominal composition of $Bi_2Se_{0.95}O_2$), on the other hand, exhibit n about two orders of magnitude larger than nominally stoichiometric samples for T_{SSR} at or below 873 K. However, n and the V_{Se} concentration are not significantly affected by T_{SSR}; instead, a reduction in grain boundary scattering explains the increase in carrier mobility and enhancement in power factor. The thermal conductivity increases slightly with T_{SSR} due to grain size growth. Cumulatively, simultaneous charge carrier concentration and mobility improvement yield a fourfold enhancement of the zT in self-doped Bi_2SeO_2, ultimately reaching $\sim$0.2 at 773 K. This study underscores the importance of systematically controlling synthesis parameters to regulate defect formation and carrier scattering in Bi_2SeO_2.

4 Methods

Experimental details

Sample preparation. Samples with the nominal composition of Bi_2SeO_2 and $Bi_2Se_{0.95}O_2$ were synthesized using two-step solid-state reaction. Commercial powders of Bi_2O_3 (Strem Chemicals, 99.9998%), Bi (Sigma-Aldrich, $\geq$99.99%), and Se (Sigma-Aldrich, 99.99%) were used as starting materials. The powders were weighed according to the stoichiometric ratio and subsequently mixed in a stainless-steel jar without milling media, using a high-energy ball mill (8000D Mixer/Mill, SPEX SamplePrep, USA) for 5 min. The obtained mixture was then cold pressed into pellets and sealed in evacuated quartz tubes. The tubes were heated to 573 K and held for 6 h, followed by subsequent heating to the temperature range from 773 K to 1173 K and held for another 12 h. Another series of samples with the nominal composition Bi_2SeO_2 was also prepared by a one-step solid-state reaction, where the sealed tubes were directly heated to temperatures ranging from 773 K to 1173 K and held for 10 h. All the obtained samples were ground to powders by hand and consolidated using spark plasma sintering (SPS; Dr. Sinter-1080, Fuji-SPS, Japan) at 903 K for 5 min in a graphite die under uniaxial pressure of 50 MPa in an Ar atmosphere. After SPS, the sintered pellets were annealed at 803 K for 6 h in an evacuated quartz tube.

Structural and morphological characterization. X-ray diffraction (XRD) patterns were collected at room temperature using a MiniFlex diffractometer (Rigaku, Japan) with a Cu-K_α radiation. The ab orientation degree for the $(00l)$ crystal planes of the bulk samples was estimated by the Lotgering method as

$$F_{(00l)} = \frac{P - P_0}{1 - P_0}, \text{ with}$$
$$P = \frac{\sum I(00l)}{\sum I(hkl)}, \text{ and } P_0 = \frac{\sum I_0(00l)}{\sum I_0(hkl)}, \tag{4}$$

where P and P_0 are the ratios of the integrated intensities of all $(00l)$ crystal planes to those of all (hkl) planes for preferentially and randomly oriented samples. $F_{(00l)} = 0$ and $F_{(00l)} = 1$ refer to completely disordered and ordered cases, respectively.[52] The morphology of the sintered samples was examined by field emission scanning electron microscopy (FESEM; Hitachi SU8230, Japan). The actual chemical composition of the samples was obtained with the aid of energy-dispersive X-ray spectroscopy (EDS; X-Max^{N} EDS detector, Horiba Scientific, Japan).

Transport properties characterization. The bulk samples were cut and polished into the required shapes and dimensions for various measurements. The Seebeck coefficient α and electrical conductivity σ were simultaneously measured on rectangular bars with dimensions of $1 \times 3 \times 8$ mm^3 using a commercial apparatus (ZEM-3, Advance Riko Inc., Japan) under a partial He pressure. The total thermal conductivity κ_{tot} was determined using the formula $\kappa_{tot} = \chi \cdot C_p \cdot d$, where χ is the thermal diffusivity, C_p is the specific heat capacity, and d is the volume density measured through the Archimedes method. The thermal diffusivity χ was measured on graphite-coated disc-shaped samples of 10 mm diameter and $\sim$1 mm thickness using the laser flash technique (LFA 467 Hyperflash, Netzsch, Germany) and analyzed using a modified Cape-Lehman model[53] with pulse correction. Simultaneously, the C_p was estimated using the comparison method with a standard sample (pyroceram-9606). The obtained C_p values were found to be in good agreement with those calculated using the Debye model. The lattice thermal conductivity κ_{lat} was calculated from κ_{tot} by subtracting the electronic contribution κ_{el} estimated according to the Wiedemann–Franz law where $\kappa_{el} = \sigma L T$. L is the Lorenz number derived from the Seebeck coefficient in the framework of the single parabolic band model with acoustic phonon scattering.[54] All transport properties were measured along the direction perpendicular to the sintering pressure. The Hall measurements were performed at room temperature using a physical properties measurement system (PPMS9T, Quantum Design Inc, USA). Electrical contacts were made with a 0.025-mm platinum wire and silver paste (Ted Pella, Inc., USA). To improve electrical contact, a thin layer of silver was pre-deposited onto the contact area. The Hall coefficient R_H was obtained from the linear fit of the Hall resistivity versus magnetic field between -5 and 5 T. The Hall carrier concentration was calculated by $n_H = 1/eR_H$, where e is the electronic charge. In principle, the Hall carrier concentration is related to the carrier concentration through $n = n_H r_H$ with r_H representing the Hall factor, which depends on the chemical potential and on the carrier scattering mechanism (see Supporting Information). Thus, free electron concentration n was estimated in the framework of the single parabolic band model, assuming acoustic phonon scattering as the main scattering mechanism for carriers. The Hall carrier mobility μ_{H} was calculated by $\mu_{\mathrm{H}} = \sigma R_{\mathrm{H}}$, where σ is the electrical conductivity. The uncertainty of the Hall measurements was estimated to be 5 – 10%, while for the Seebeck coefficient, it was estimated to be 6%, 8% for the electrical conductivity, 11% for the thermal conductivity, and 16% for the figure of merit zT.[55]

Computational details

Density functional theory (DFT) calculations were performed using the Vienna *Ab initio* Simulation Package (VASP)[56,57] under the projector-augmented wave formalism.[58,59] An energy cutoff of 340 eV was used in all calculations.

Since Bi_2SeO_2 has a layered structure with space group $I4/mmm$, the generalized gradient approximation (GGA) of Perdew-Burke-Ernzerhof (PBE) overestimates the c axis by 1.2% (Table S2) due to the underbinding of layers in quasi-2D structures by GGA.[60] We therefore use the vdW-corrected optB86 (vdW) functional[61] to relax all structures related to Bi_2SeO_2 (bulk, defects, etc.). As shown in Table S2, the lattice constants are in much better agreement with experiments with the vdW functional. The electronic structure of Bi_2SeO_2 was calculated using the HSE06 functional with spin-orbit coupling on the vdW-relaxed structure, as suggested by Marom et al.[62] The density of states was calculated using the tetrahedron method[63] and a Γ-centered $8 \times 8 \times 4$ grid for k-point integration.[64] The calculated band gap is $E_g = 0.857$ eV, in agreement with the experimental band gap of 0.8 – 0.9 eV.[36,65,66]

All point defect calculations were performed on a $3 \times 3 \times 2$ supercell of Bi_2SeO_2 (containing 90 atoms total). A two-step computational process was undertaken, where structural relaxations were performed using the vdW functional and, subsequently, the total energies were calculated using HSE06. A similar approach was taken in a previous study of point defect chemistry in layered BiCuSeO,[9] where fair agreement with experimental carrier concentrations was observed. The formation energy ΔE_{D^q} of a defect D with charge state q was calculated using the formula[67]

$$\Delta E_{\mathrm{D}^q} = E_{\mathrm{D}^q} - E_{\mathrm{host}} - \sum_i n_i \mu_i + qE_{\mathrm{F}} + E_{\mathrm{corr}} \tag{5}$$

where E_{D^q} and E_{host} are the total energies of the supercell with and without the defect, respectively, μ_i is the chemical potential of an atom that is either added ($n_i > 0$) or removed ($n_i < 0$) to created defect D, E_{F} is the Fermi energy, and E_{corr} is a correction to the formation energy arising from finite-size effects of the supercell approach. We represent the chemical potential of each element as a deviation from a reference state, i.e., $\mu_i = \mu_i^0 + \Delta\mu_i$, where the elemental reference energy μ_i^0 was fit to a set of experimentally-measured formation enthalpies of several compounds under standard conditions (Table S3).[68] The deviation from the reference energy, $\Delta\mu_i$, is determined by the thermodynamic conditions of the system. Since Bi_2SeO_2 is in thermodynamic equilibrium with different secondary phases depending on the initial synthesis conditions of the sample, $\Delta\mu_i$ of each elements will also differ (Table S1); for example, if Bi_2SeO_2 is in equilibrium with Bi_2O_3 and elemental Bi (i.e., the most Se-poor condition), then the chemical potentials $\Delta\mu_i$ are determined by the following set of equations:

$$\begin{gathered} 2\Delta\mu_{\mathrm{Bi}} + 2\Delta\mu_{\mathrm{O}} + \Delta\mu_{\mathrm{Se}} = \Delta H_{\mathrm{f}}^{\mathrm{Bi_2SeO_2}} \\ \Delta\mu_{\mathrm{Bi}} = \Delta H_{\mathrm{f}}^{\mathrm{Bi}} (= 0) \\ 2\Delta\mu_{\mathrm{Bi}} + 3\Delta\mu_{\mathrm{O}} = \Delta H_{\mathrm{f}}^{\mathrm{Bi_2O_3}} \end{gathered} \tag{6}$$

Since we assumed a dilute-limit model, corrections arising from finite-size effects, i.e., E_{corr}, were also considered.[69] Due to the finite supercell size used in our defect calculations, we considered energy corrections arising from three factors: (i) long-range interactions between image charges across periodic boundaries, (ii) misalignment of the average electrostatic potential between the system with and without the defect, and (iii) Moss-Burstein-type band filling of shallow defects.[70]

The free charge carrier concentrations were calculated following the charge neutrality condition

$$\sum_{\mathrm{D}^q} \left[qN_{\mathrm{D}} \mathrm{e}^{-\Delta E_{\mathrm{D}^q}/k_B T} \right] + p - n = 0 \tag{7}$$

where N_{D} is the site concentration, k_{B} is the Boltzmann constant, and T is the synthesis temperature. The free hole (p) and electron (n) concentrations are calculated using the density-of-states $g(E)$ and the Fermi-Dirac distribution $f(E)$ as

$$\begin{aligned} p &= \int_{-\infty}^{\mathrm{VBM}} g(E) \left[1 - f(E)\right] dE, \\ n &= \int_{\mathrm{CBM}}^{\infty} g(E) f(E) dE. \end{aligned} \tag{8}$$

Acknowledgements

T.M., A.N., and I.S. acknowledge JST Mirai JPMJMI19A1 and JST SPRING JPMJSP2124. M.Y.T. is funded by the United States Department of Energy through the Computational Science Graduate Fellowship (DOE CSGF) under grant number DE-SC0020347. M.Y.T. also acknowledges support from the Johannes and Julia Randall Weertman Graduate Fellowship. M.Y.T. and G.J.S. acknowledges the support of award 70NANB19H005 from U.S. Department of Commerce, National Institute of Standards and Technology as part of the Center for Hierarchical Materials Design (CHiMaD). P.G. acknowledges support from NSF through award DMR-2102409. The research was performed using computational resources sponsored by DOE's Office of Energy Efficiency and Renewable Energy and located at the NREL. A part of this work was supported by "Advanced Research Infrastructure for Materials and Nanotechnology in Japan (ARIM)" of the Ministry of Education, Culture, Sports, Science and Technology (MEXT); proposal number JPMXP1224NM5121.

CRediT Statement

Andrei Novitskii: Conceptualization, Methodology, Investigation, Data Curation, Writing (Original Draft). **Michael Toriyama**:

Conceptualization, Investigation, Data Curation, Writing (Original Draft). **Illia Serhiienko**: Investigation, Writing (Editing). **Takao Mori**: Writing (Editing), Resources, Supervision, Funding Acquisition. **G. Jeffrey Snyder**: Writing (Editing), Supervision. **Prashun Gorai**: Conceptualization, Writing (Editing), Supervision, Project Administration.

Conflicts of Interest

There are no conflicts to declare.

Data Availability Statement

The data that supports the findings of this study are available within the article and its supplementary material.

References

1 A. F. Ioffe, *Semiconductor Thermoelements, and Thermoelectric Cooling*, Infosearch, 1957.

2 J. Zheng, D. Wang and L.-D. Zhao, *Materials*, 2021, **14**, 3905.

3 S. Tippireddy, P. K. DS, S. Das and R. C. Mallik, *ACS Appl. Energy Mater.*, 2021, **4**, 2022–2040.

4 G.-K. Ren, J.-L. Lan, L.-D. Zhao, C. Liu, H. Yuan, Y. Shi, Z. Zhou and Y.-H. Lin, *Mater. Today*, 2019, **29**, 68–85.

5 M. Dutta, D. Sarkar and K. Biswas, *Chem. Commun.*, 2021, **57**, 4751–4767.

6 L.-D. Zhao, J. He, D. Berardan, Y. Lin, J.-F. Li, C.-W. Nan and N. Dragoe, *Energy Environ. Sci.*, 2014, **7**, 2900–2924.

7 Y. Liu, L.-D. Zhao, Y. Zhu, Y. Liu, F. Li, M. Yu, D.-B. Liu, W. Xu, Y.-H. Lin and C.-W. Nan, *Adv. Energy Mater.*, 2016, **6**, 1502423.

8 L. Pan, Y. Lang, L. Zhao, D. Berardan, E. Amzallag, C. Xu, Y. Gu, C. Chen, L.-D. Zhao, X. Shen, Y. Lyu, C. Lu and Y. Wang, *J. Mater. Chem. A*, 2018, **6**, 13340–13349.

9 M. Y. Toriyama, J. Qu, G. J. Snyder and P. Gorai, *J. Mater. Chem. A*, 2021, **9**, 20685–20694.

10 Z. Zhou, X. Tan, G. Ren, Y. Lin and C. Nan, *J. Electron. Mater.*, 2017, **46**, 2593–2598.

11 X. Zhang, D. Feng, J. He and L.-D. Zhao, *J. Solid State Chem.*, 2018, **258**, 510–516.

12 X. Zhang, D. Wang, G. Wang and L.-D. Zhao, *Ceram. Int.*, 2019, **45**, 14953–14957.

13 S. Tan, C. Gao, C. Wang, Y. Sun, Q. Jing, Q. Meng, T. Zhou and J. Ren, *Solid State Sci.*, 2019, **98**, 106019.

14 X. Ding, M. Li, P. Chen, Y. Zhao, M. Zhao, H. Leng, Y. Wang, S. Ali, F. Raziq, X. Wu, H. Xiao, X. Zu, Q. Wang, A. Vinu, J. Yi and L. Qiao, *Matter*, 2022, **5**, 4274–4314.

15 L. Pan, L. Zhao, X. Zhang, C. Chen, P. Yao, C. Jiang, X. Shen, Y. Lyu, C. Lu, L.-D. Zhao and Y. Wang, *ACS Appl. Mater. Interfaces*, 2019, **11**, 21603–21609.

16 N. Yang, L. Pan, C. Chen and Y. Wang, *J. Alloys Compd.*, 2021, **858**, 157748.

17 X. Tan, J.-L. Lan, K. Hu, B. Xu, Y. Liu, P. Zhang, X.-Z. Cao, Y. Zhu, W. Xu, Y.-H. Lin and C.-W. Nan, *J. Am. Ceram. Soc.*, 2018, **101**, 4634–4644.

18 R. Liu, X. Tan, Y.-C. Liu, G.-K. Ren, C. Liu, Z.-F. Zhou, C.-W. Nan and Y.-H. Lin, *J. Eur. Ceram. Soc.*, 2018, **38**, 2742–2746.

19 P. Ruleová, T. Plechacek, J. Kasparova, M. Vlcek, L. Benes, P. Lostak and C. Drasar, *J. Electron. Mater.*, 2018, **47**, 1459–1466.

20 B. Zhan, S. Butt, Y. Liu, J.-L. Lan, C.-W. Nan and Y.-H. Lin, *J. Electroceram.*, 2015, **34**, 175–179.

21 C. Song, Y. Song, L. Pan, C. Chen, P. Zong and Y. Wang, *J. Alloys Compd.*, 2022, **892**, 162147.

22 H. Hong, D. Kim, S. Won and K. Park, *J. Mater. Res. Technol.*, 2021, **15**, 4161–4172.

23 Y. Li, H. Huo, H. Huang, K. Guo, X. Yang, J. Xing, J. Luo, G.-H. Rao and J.-T. Zhao, *J. Mater. Sci.*, 2021, **56**, 12732–12739.

24 M. Kim, D. Park and J. Kim, *J. Alloys Compd.*, 2021, **851**, 156905.

25 X. Tan, Y. Liu, R. Liu, Z. Zhou, C. Liu, J.-L. Lan, Q. Zhang, Y.-H. Lin and C.-W. Nan, *Adv. Energy Mater.*, 2019, **9**, 1900354.

26 L. Pan, Z. Zhao, N. Yang, W. Xing, J. Zhang, Y. Liu, C. Chen, D. Li and Y. Wang, *J. Eur. Ceram. Soc.*, 2020, **40**, 5543–5548.

27 X. Tan, Y. Liu, K. Hu, G. Ren, Y. Li, R. Liu, Y.-H. Lin, J.-L. Lan and C.-W. Nan, *J. Am. Ceram. Soc.*, 2018, **101**, 326–333.

28 L. Pan, W.-D. Liu, J.-Y. Zhang, X.-L. Shi, H. Gao, Q.-F. Liu, X. Shen, C. Lu, Y.-F. Wang and Z.-G. Chen, *Nano Energy*, 2020, **69**, 104394.

29 X. Tan, J.-l. Lan, G. Ren, Y. Liu, Y.-H. Lin and C.-W. Nan, *J. Am. Ceram. Soc.*, 2017, **100**, 1494–1501.

30 Z.-H. Zheng, T. Wang, B. Jabar, D.-W. Ao, F. Li, Y.-X. Chen, G.-X. Liang, J.-T. Luo and P. Fan, *ACS Appl. Energy Mater.*, 2021, **4**, 10290–10297.

31 S. Ohno, K. Imasato, S. Anand, H. Tamaki, S. D. Kang, P. Gorai, H. K. Sato, E. S. Toberer, T. Kanno and G. J. Snyder, *Joule*, 2018, **2**, 141–154.

32 M. Shimoda, M. Maegawa, S. Yoshida, H. Akamatsu, K. Hayashi, P. Gorai and S. Ohno, *Chem. Mater.*, 2022, **34**, 5634–5643.

33 C.-W. Lee, N. U. Din, G. L. Brennecka and P. Gorai, *Appl. Phys. Lett.*, 2024, **125**, 022901.

34 J. J. Kuo, Y. Yu, S. D. Kang, O. Cojocaru-Mirédin, M. Wuttig and G. J. Snyder, *Adv. Mater. Interfaces*, 2019, **6**, 1900429.

35 C. Drasar, P. Ruleova, L. Benes and P. Lostak, *J. Electron. Mater.*, 2012, **41**, 2317–2321.

36 C. Chen, M. Wang, J. Wu, H. Fu, H. Yang, Z. Tian, T. Tu, H. Peng, Y. Sun, X. Xu, J. Jiang, N. B. M. Schröter, Y. Li, D. Pei, S. Liu, S. A. Ekahana, H. Yuan, J. Xue, G. Li, J. Jia, Z. Liu, B. Yan, H. Peng and Y. Chen, *Sci. Adv.*, 2018, **4**, eaat8355.

37 Q. Mao, X. Geng, J. Yang, J. Zhang, S. Zhu, Q. Yu, Y. Wang, H. Li, R. Li and H. Hao, *J. Cryst. Growth*, 2018, **498**, 244–247.

38 J. Wang, W. Hu, Z. Lou, Z. Xu, X. Yang, T. Wang and X. Lin, *Appl. Phys. Lett.*, 2021, **119**, 081901.

39 L. Xu, Y.-C. Luo, Y.-Y. Lv, Y.-Y. Zhang, Y.-Z. Wu, S.-H. Yao, J. Zhou, Y. Chen and Y.-F. Chen, *J. Phys. Condens. Matter.*, 2020, **32**, 365705.

40 H. Boller, *Monatsh. Chem.*, 1973, **104**, 916–919.

41 A. L. Pereira, D. Errandonea, A. Beltran, L. Gracia, O. Gomis, J. A. Sans, B. García-Domene, A. Miquel-Veyrat, F. Manjón,

A. Muñoz and C. Popescu, *J. Phys. Condens. Matter.*, 2013, **25**, 475402.

42 J. Sui, J. Li, J. He, Y.-L. Pei, D. Berardan, H. Wu, N. Dragoe, W. Cai and L.-D. Zhao, *Energy Environ. Sci.*, 2013, **6**, 2916–2920.

43 Z. Zhao, J. Zheng, Y. Li, S. Wang, S. Liu, S. Zhan, L. Wang, X. Zhang and L.-D. Zhao, *Nano Energy*, 2024, 109649.

44 L. Pan, J. Zhang, C. Chen and Y. Wang, *Scripta Mater.*, 2020, **178**, 376–381.

45 G. J. Snyder, A. H. Snyder, M. Wood, R. Gurunathan, B. H. Snyder and C. Niu, *Adv. Mater.*, 2020, **32**, 2001537.

46 J. J. Kuo, S. D. Kang, K. Imasato, H. Tamaki, S. Ohno, T. Kanno and G. J. Snyder, *Energy Environ. Sci.*, 2018, **11**, 429–434.

47 M. T. Dylla, J. J. Kuo, I. Witting and G. J. Snyder, *Adv. Mater. Interfaces*, 2019, **6**, 1900222.

48 D. G. Cahill, S. K. Watson and R. O. Pohl, *Phys. Rev. B*, 1992, **46**, 6131.

49 R. Gurunathan, R. Hanus and G. J. Snyder, *Mater. Horiz.*, 2020, **7**, 1452–1456.

50 R. Gurunathan, R. Hanus, M. Dylla, A. Katre and G. J. Snyder, *Phys. Rev. Appl.*, 2020, **13**, 034011.

51 R. Chasmar and R. Stratton, *Int. J. Electron.*, 1959, **7**, 52–72.

52 F. Lotgering, *J. Inorg. Nucl. Chem.*, 1959, **9**, 113–123.

53 J. Cape and G. Lehman, *J. Appl. Phys.*, 1963, **34**, 1909–1913.

54 H.-S. Kim, Z. M. Gibbs, Y. Tang, H. Wang and G. J. Snyder, *APL Mater.*, 2015, **3**, 041506.

55 E. Alleno, D. Bérardan, C. Byl, C. Candolfi, R. Daou, R. Decourt, E. Guilmeau, S. Hébert, J. Hejtmánek, B. Lenoir, P. Masschelein, V. Ohorodnichuk, M. Pollet, S. Populoh, D. Ravot, O. Rouleau and M. Soulier, *Rev. Sci. Instrum.*, 2015, **86**, 011301.

56 G. Kresse and J. Furthmüller, *Comput. Mater. Sci.*, 1996, **6**, 15–50.

57 G. Kresse and J. Furthmüller, *Phys. Rev. B*, 1996, **54**, 11169.

58 P. E. Blöchl, *Phys. Rev. B*, 1994, **50**, 17953.

59 G. Kresse and D. Joubert, *Phys. Rev. B*, 1999, **59**, 1758.

60 P. Gorai, E. S. Toberer and V. Stevanović, *J. Mater. Chem. A*, 2016, **4**, 11110–11116.

61 J. Klimeš, D. R. Bowler and A. Michaelides, *Phys. Rev. B*, 2011, **83**, 195131.

62 N. Marom, A. Tkatchenko, M. Scheffler and L. Kronik, *J. Chem. Theory Comput.*, 2010, **6**, 81–90.

63 P. E. Blöchl, O. Jepsen and O. K. Andersen, *Phys. Rev. B*, 1994, **49**, 16223.

64 H. J. Monkhorst and J. D. Pack, *Phys. Rev. B*, 1976, **13**, 5188.

65 J. Wu, H. Yuan, M. Meng, C. Chen, Y. Sun, Z. Chen, W. Dang, C. Tan, Y. Liu, J. Yin, Y. Zhou, S. Huang, H. Q. Xu, Y. Cui, H. Y. Hwang, Z. Liu, Y. Chen, B. Yan and H. Peng, *Nat. Nanotechnol.*, 2017, **12**, 530–534.

66 J. Yin, Z. Tan, H. Hong, J. Wu, H. Yuan, Y. Liu, C. Chen, C. Tan, F. Yao, T. Li, Y. Chen, Z. Liu, K. Liu and H. Peng, *Nat. Commun.*, 2018, **9**, 1–7.

67 S. Lany and A. Zunger, *Modell. Simul. Mater. Sci. Eng.*, 2009, **17**, 084002.

68 V. Stevanović, S. Lany, X. Zhang and A. Zunger, *Phys. Rev. B*, 2012, **85**, 115104.

69 S. Lany and A. Zunger, *Phys. Rev. B*, 2008, **78**, 235104.

70 E. Burstein, *Phys. Rev.*, 1954, **93**, 632.